JOURNAL OF PROPULSION AND POWER
Vol. 27, No. 2, March–April 2011

Supersonic Fin–Body Interactions in an Internal Scramjet Flow

Philippe Lorrain* and Russell Boyce†
University of Queensland, Brisbane, Queensland 4072, Australia

DOI: 10.2514/1.49226

This paper reports on the study of a fin–body junction flow in the context of an internal scramjet flowpath. Three-dimensional Reynolds-averaged Navier–Stokes numerical simulations of the flowfield inside a particular scramjet configuration have been performed using the commercial computational fluid dynamics code CFD++. The junction is formed by a central strut fuel injector spanning the entrance to a direct-connect combustor. The local flow Mach number is 2.5. The bow shock generated by the blunt strut injector causes flow separation on the side wall, which leads to the formation of horseshoe vortices. The computed results in the symmetry plane and on the injector surface near the leading edge of the strut are in good agreement with the solutions obtained by other investigators for isolated fin–body junctions. Further downstream, reflections of the strut bow shock at the internal flow top wall and then the strut surface have significant effect on the propagation of the fin–body interaction. The shock–vortex interaction was found to despin the primary horseshoe vortex; i.e., oppositely orientated vorticity is induced, and hence dissipate vorticity. Further reduction of the vorticity, associated with the observed vortices, occurs due to viscous dissipation of the horseshoe vortices in the internal flow side wall boundary layer.

Nomenclature

D	=	nose diameter of central strut injector
h	=	enthalpy
k	=	turbulence kinetic energy
M	=	Mach number
p	=	pressure
R	=	specific gas constant
T	=	temperature
u, v, w	=	velocity component in x-direction
x, y, z	=	global model coordinates
y^+	=	dimensionless wall distance in y-direction, $(\tau_{\text{wall}}/\rho)^{1/2}$
γ	=	ratio of specific heats, c_p/c_v
ε	=	specific dissipation rate (k-ε turbulence model)
ν	=	undamped eddy viscosity (Spalart–Allmaras turbulence model)
ρ	=	density
Φ	=	angle on strut injector nose

Subscripts

$t2$	=	pitot condition
wall	=	evaluated at the wall
0	=	stagnation condition
∞	=	freestream condition

I. Introduction

A METHOD commonly used for scramjet fuel injection is central strut injection. An advantage of employing this kind of device is that the fuel is injected in the streamwise direction, contributing to the overall thrust production. However, central strut injectors spanning the flow passage inside a scramjet engine feature fin–body junctions at the walls, and will thus display the three-dimensional separation phenomena associated with supersonic fin–body interactions. It is important to understand the physical aspects of such three-dimensional separated flows.

Extensive research has been carried out both experimental [1–4] and numerical [5–11] to investigate the characteristics inherent to fin–body junction flowfields. A schematic of the physical model, taken from [6], is given in Fig. 1. Commonly, the following flowfield is assumed. The bow shock generated in front of the blunt fin acts to separate the oncoming boundary layer on the body surface, resulting in the formation of a λ-type shock pattern in the plane of symmetry upstream of the fin leading edge, and locally high heat transfer rates and pressures on the fin leading edge. Pressure measurements and evaluation of surface oil flow patterns, derived from experimental investigations of hemispherical blunted fins mounted on a flat plate [1–4], have revealed that the shock-induced separation is governed by the fin diameter D for a wide range of Mach numbers and incoming boundary layer thicknesses. The maximum upstream influence of the separation has been found to range between 2 and 3 times this diameter, for all cases investigated. The separated region below this shock structure is composed of horseshoe vortices which are continually fed with high momentum freestream flow and spiral downstream around the nose of the fin. This type of interaction is commonly referred to as Edney-type 4 interference [6,7]. Therefore, starting from the corner of a fin–body junction, a highly three-dimensional flowfield is created downstream of the junction.

Previous investigations have been focused on a detailed description of the interaction characteristics upstream of the fin; on the body surface and in the plane of symmetry. Hung and Buning [7] present the only study in which the three-dimensional flowfield around the nose of the blunt fin is investigated in more detail. However, little work has been done concerning the downstream development of the observed vortices. Furthermore, the published work considers fin–body junctions in isolation, setting the outer boundaries far enough away so as to exclude any influences on the interaction phenomena. For the case of a central strut fuel injector inside a scramjet engine, however, the bow shock is able to reflect at the main wall and returns to the injector surface, interacting further with the fin–body interaction phenomena. This brings about additional shock wave/boundary-layer interactions (SWBLIs) and shock–vortex interactions (SVIs), which significantly increase the complexity of the disturbed flowfield. The aim of the present work is to employ high resolution computational fluid dynamics (CFD) to determine the internal fin–body junction flow structures for a specific scramjet strut injection flowfield that has been reported previously [12]. The numerical simulations are carried out by solving the three-dimensional Reynolds-averaged Navier–Stokes (RANS) equations

Presented as Paper 2009-7251 at the 16th AIAA/DLR/GGLR International Spaceplanes and Hypersonic Systems and Technologies Conference, Bremen, Germany, 19–22 October 2009; received 5 February 2010; revision received 4 August 2010; accepted for publication 29 September 2010.

*Postgraduate Student, Center for Hypersonics. Student Member AIAA.
†Professor, Center for Hypersonics. Senior Member AIAA.

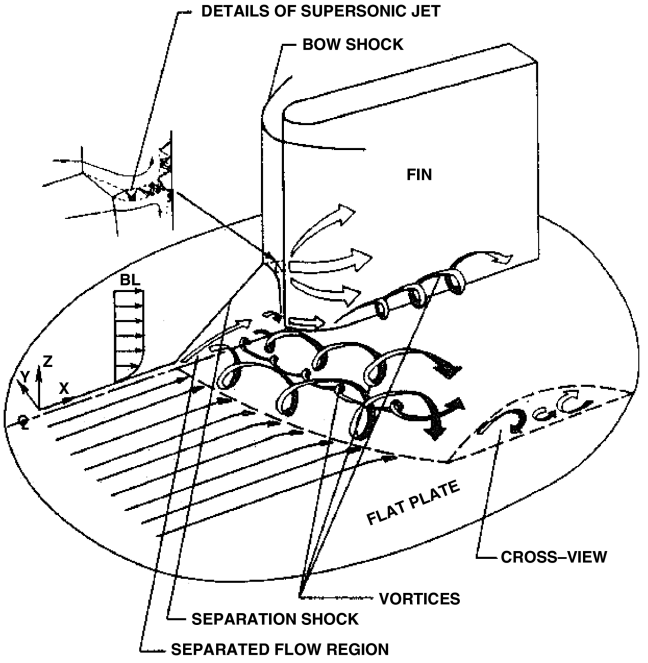

Fig. 1 Simplified sketch of blunt-fin-induced SWBLI [6].

for a compressible perfect gas flow. This approach is reasonable as, despite the inherent unsteadiness of the λ-shock structure observed in experiments, the characteristic junction flow features were found to remain unaltered for the time-averaged flowfield [3,4].

II. Scramjet Strut Injection Configuration

The computational model used for the present study is based on a particular nominally two-dimensional scramjet configuration tested by Boyce et al. [12], Fig. 2. The configuration consists of: a pair of opposed ramps inclined by 25.8°, which serves as the inlet; a rectangular throat section; a Mach 2.5 nozzle; and a combustion chamber. Fuel injection was achieved by a central strut fuel injector spanning the entrance to the combustion chamber at the exit of the nozzle. The strut injector consists of a blunt nosed wedge of 5° half-angle followed by a plane segment (see detail in Fig. 2). The nose radius is 1 mm. The fuel was fed through circular portholes inside the plane part of the strut injector and then injected sonically from the rear via a nozzle slot with a throat height of 1.6 mm. The inlet was designed as an unstarted inlet aimed at enforcing the formation of a bow shock in front of the inlet in order to provide a stagnant reservoir for the Mach 2.5 nozzle; hence to achieve the desired flow conditions at the combustor entrance for a facility comparison study. The working principle of establishing this flow is sketched in Fig. 3. Oblique shock waves, generated at the tips of the intake ramps, impinge on the opposite ramp surfaces upstream of the trailing edges and on the parallel side wall. The strong adverse pressure gradient imposed by the incident shock waves acts to separate the boundary layers on the inlet ramps and on the side walls causing additional separation shocks which further contribute to the compression process. Eventually, the flow within the inlet becomes chocked, inducing a normal shock wave (Mach reflection) that travels upstream of the intake to form a curved bow shock. The shock tunnel operating conditions were chosen such that the desired flow stagnation conditions prevailed behind the bow shock. Successful operation of this configuration was reported in [13]. The scramjet freestream and nozzle exit conditions obtained in the experiments, and derived from a combination of experimental measurement and numerical simulation, are compiled in Table 1. These serve as the reference data set for the present computations. A detailed study concerning the determination of the flow conditions is given in [13].

III. Numerical Method

A. CFD++

The commercial CFD code CFD++ [14] was used for the present calculations. CFD++ can solve both the steady and unsteady, i.e., time-accurate, three-dimensional Navier–Stokes equations for compressible flows, including multispecies and finite-rate chemistry modeling. Viscous effects are specified according to the Sutherland law approximation. The chosen set of equations are the three-dimensional compressible perfect gas Navier–Stokes equations. Turbulence modeling was carried out by solving the RANS equations and employing the one-equation Spalart–Allmaras (SA) and the two-equation k-ε turbulence models, with a freestream turbulence level of 2%. With all calculations, turbulence production and dissipation terms were corrected to include compressibility effects using the proprietary method formulated for CFD++. The correction approach used was that for wall-bounded flows, which compensates for compressibility by reducing turbulence kinetic energy production. Its main advantage is that it accounts for the reduction of turbulence generation as a wall is approached.

CFD++ is basically an unstructured code, but handles Cartesian structured curvilinear and unstructured grids, including hybrids. The calculations performed were double precision and of second-order accuracy in both time and space. Regarding the spatial discretization, total variation diminishing polynomial interpolation with MinMod

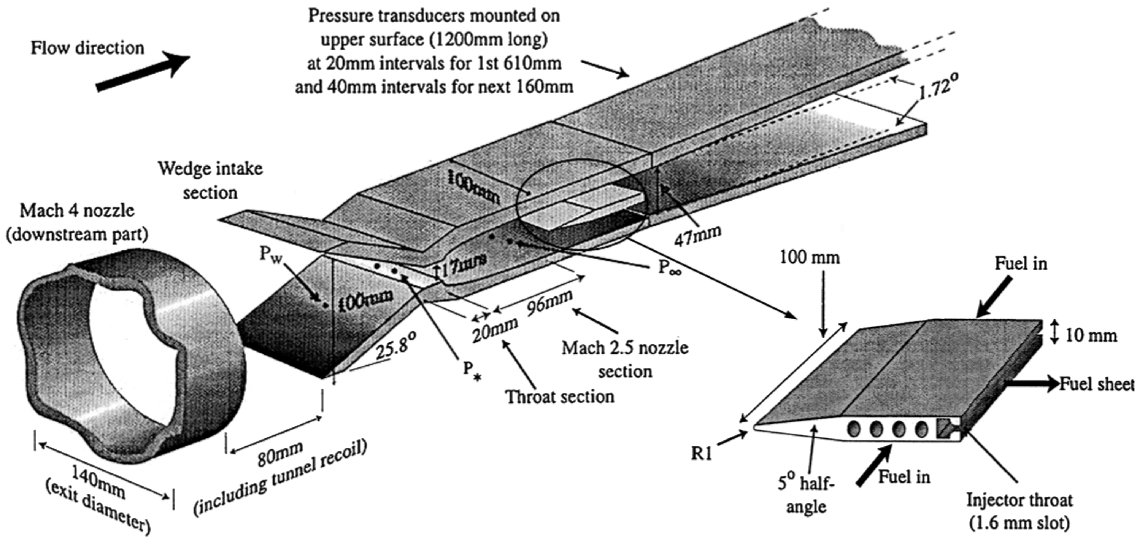

Fig. 2 Experimental scramjet configuration tested by Boyce et al. [12].

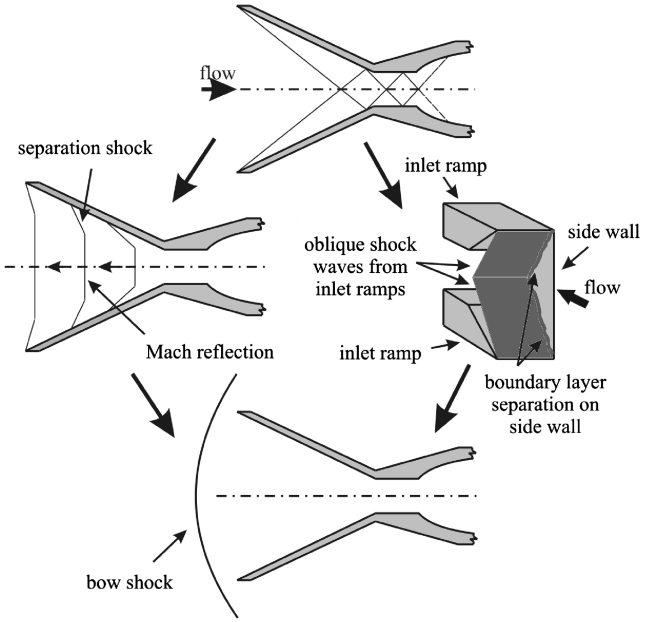

Fig. 3 Schematic of inlet unstart process.

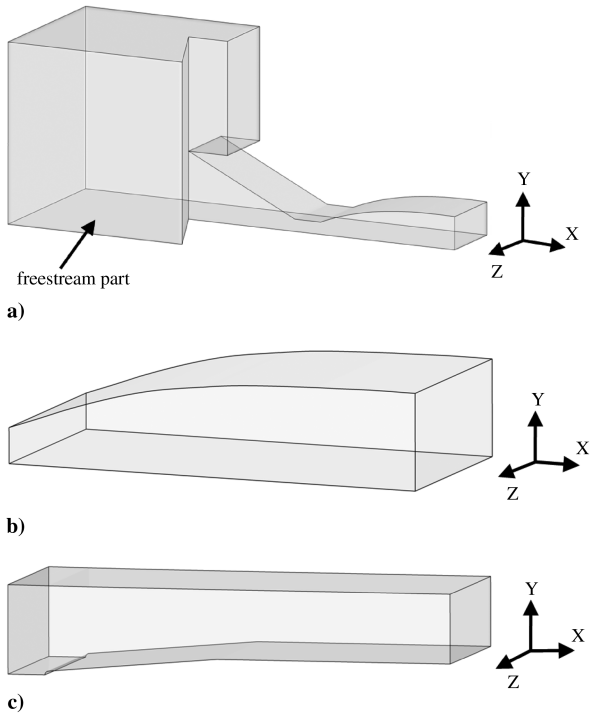

Fig. 4 Computational models: a) laminar inlet/nozzle model, b) turbulent nozzle model, and c) turbulent injector domain model.

limiting was used, while an implicit Runge-Kutta method was applied for the time integration. For the near-wall closure, the solve-to-the-wall method was employed. The finite-volume method that is implemented in CFD++ is based on an approximation of the surface and volume integrals of the governing Navier–Stokes equations at the centroids of each control volume (CV) of the computational mesh whereby algebraic equations between the CVs are obtained. The same polynomial was used in computing viscous fluxes. Inviscid fluxes were calculated using the Harten, Lax and Van Leer with contact discontinuity nonlinear approximate Riemann solver with advanced multidimensional polynomial reconstruction to high order.

CFD++ has had considerable investment concerning code validation and has been used with great success ranging from ramp flow calculations [15] to combustion simulations [16]. The reader is referred to various works in the literature for further information on the code and code validation (see for example [17]).

For all calculations, the steady state solution strategy was applied. The CFD++ computations were performed on an Intel Itanium2 Linux cluster provided by Australia's National Computational Infrastructure National Facility.

B. Mesh System

The scramjet geometry, excluding the combustion chamber, has been accurately modeled in three-dimensional space using hexahedral (structured) elements. The grids were generated using the commercial software Gridgen [18].

Figures 4a–4c show the different meshes used for the present computations. Taking advantage of the symmetric, nominally two-dimensional design of the original scramjet configuration, only one quarter of the configuration was modeled. Hence, each computational model contains two symmetry planes. A freestream part was added upstream of the inlet to capture the three-dimensional extension of the bow shock wave around the inlet. The inlet, up to the exit of the nozzle, and the injector domain were computed separately to allow for an enhanced mesh resolution of either model. Grid point clustering was applied towards the walls, and the first grid point spacing at each solid surface was set to 1×10^{-6} to achieve a distribution of y^+ at the wall that remains of order unity for the entire surface; hence to provide an accurate resolution of the turbulent boundary layer. Furthermore, the flow was assumed to be laminar up to the end of the throat. Then, a separate turbulent nozzle calculation was performed using the model shown in Fig. 4b. This helped overcome convergence problems caused by the highly unsteady unstart process of the inlet. Preliminary two-dimensional calculations comparing distributions along the wall between fully turbulent (intake plus nozzle) and laminar intake/turbulent nozzle computations provided justification for this approach: pressure distributions were almost identical, and heat flux distributions converged by the end of the nozzle.

A mesh sensitivity study has been carried out for the turbulent (SA and k-ε) nozzle computations using three different grids, $120 \times 74 \times 94$ (coarse), $190 \times 99 \times 129$ (medium), and $190 \times 129 \times 169$ (fine), in order to ensure that the computed nozzle exit conditions are not affected by insufficient mesh resolution. For the sake of brevity, only selected results of the grid refinement study are presented in this paper. Comparisons of the distribution of the dimensionless wall distance, y^+, along the nozzle contour in the (x-y)-symmetry plane for the SA solution are shown in Fig. 5. The variations between the different meshes are minor. The y^+ values gradually decrease and remain below unity towards the exit of the nozzle indicating a meaningful resolution of the turbulent boundary layer and its viscous sublayer. Additionally, the distribution was found to be uniform in the spanwise direction. The same degree of mesh convergence was observed for the y^+ distributions on the side wall of the nozzle (not shown here). Figure 6 shows the Mach number profiles at the nozzle exit in both symmetry planes. The value specified for the experiments and its corresponding uncertainty band are included for comparison. The agreement is good and the solution is mesh converged. Based on these results, the medium mesh results were used to supply inflow profiles for the subsequent injector domain computations.

Table 1 Mach 2.5 nozzle freestream conditions specified for T4 experiments [12]

Parameter	Unit	Value
p_0	kPa	$1035 \pm 1\%$ (meas.)
T_0	K	$2105 \pm 6\%$
h_0	MJ/kg	$2.40 \pm 6\%$
p_∞	kPa	$59 \pm 9\%$ (meas.)
T_∞	K	$1025 \pm 13\%$
u_∞	m/s	$1560 \pm 4\%$
M_∞	——	$2.47 \pm 6\%$
γ_∞	——	1.39 ± 0.01
R_∞	J/kg K	287.1

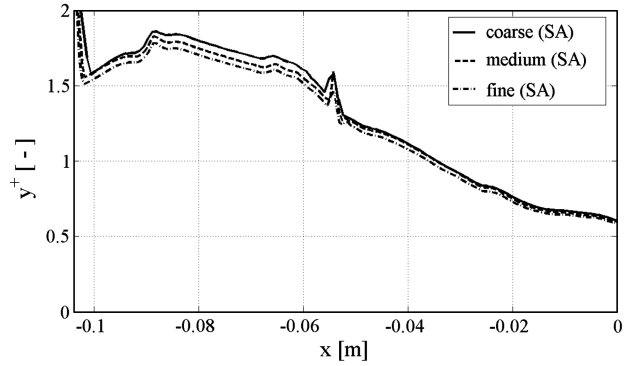

Fig. 5 Grid dependence of y^+ distribution along the nozzle contour in (x-y)-symmetry plane for turbulent (SA) nozzle computations.

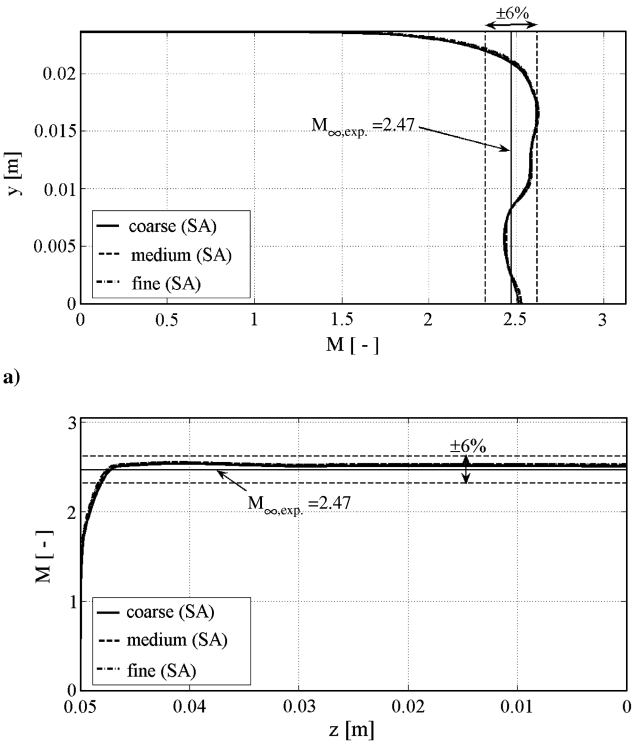

Fig. 6 Grid dependence of Mach number profiles at nozzle exit (SA solution): a) (x-y)-symmetry plane and b) (x-z)-symmetry plane.

For the turbulent strut injector domain computations, two different grids, $343 \times 178 \times 150$ (coarse) and $593 \times 283 \times 298$ (fine), were used to assess the effect of mesh resolution on the characteristics of the SWBLIs at the injector/side wall junction and at the subsequent shock reflections at the top wall and the injector surface. A detailed discussion is given in Sec. III.

C. Boundary Conditions

The shock tunnel freestream properties reached in the experiments are taken as uniform inflow conditions for the unstarted inlet simulations. The corresponding values are compiled in Table 2. User-defined three-dimensional inflow profiles were then used for the turbulent nozzle and injector domain calculations. These include information about the primitive flow variables p, T, u, v, w, and the respective turbulent quantities; undamped eddy viscosity ν (SA), and turbulence kinetic energy k (k-ε) and specific dissipation rate ε (k-ε). For the supersonic outflow, at the nozzle exit and at the downstream end of the injector domain, the flow variables are extrapolated from the interior.

The strut injector is flush mounted to the parallel side walls of the scramjet duct. A symmetry condition is imposed at both planes of symmetry of each grid [(x-y) and (x-z) planes in Fig. 4]. A no-slip and an isothermal wall condition, assuming $T_{\text{wall}} = 300$ K, are specified at each solid surface. The latter assumption arises from the very short test time in the experiments, of the order of milliseconds, which is insufficient to cause significant elevation of the surface temperature relative to the total temperature of the flow.

Previous investigations of isolated fin–body junction flows revealed an upstream extent of the separation on the body surface ranging between 2 and 3 times the leading-edge diameter of the fin, D [1–4]. For the present geometry, the nose diameter of the blunt strut injector is $D = 2$ mm. However, this correlation was found for a uniform distribution of the flow variables at the inflow boundary of the flow domain upstream of the fin leading edge. Accounting for potential nonuniformities in the distribution of the flow variables at the nozzle exit, which provide the inflow conditions for the injector domain computations, the inflow boundary of the injector domain was placed 10 mm upstream of the leading edge of the injector in order to capture the upstream influence of the shock-induced separation on the side wall.

IV. Results and Discussion

A. Inflow to the Fin–Body Interaction Region: Inlet/Nozzle Results

A laminar computation of the unstarted inlet and the nozzle was initiated at first. Subsequently, turbulent computations of the expansion within the Mach 2.5 nozzle were conducted. Figure 7 displays the Mach number distribution in the (x-y)-symmetry plane of the three-dimensional inlet/nozzle domain mirrored at the x-axis. The bow shock in front of the inlet is clearly discernible. Behind the bow shock, an almost stagnant flow region is established which provides the reservoir for the Mach 2.5 nozzle.

Figure 8 shows the wall pressure distribution along the top wall (a) and the Mach number distribution on the centerline (b) of the inlet/nozzle domain both in the (x-y)-symmetry plane for the laminar inlet/nozzle and turbulent (SA and k-ε) nozzle computations. The experimental wall pressure measurements [12] along with the corresponding uncertainty ranges are included, for comparison, indicating good agreement between CFD and experiments. Starting at approximately 1 MPa (desired total pressure for scramjet model flow) behind the bow shock, the pressure in the inlet decreases in the streamwise direction (positive x-direction) due to flow acceleration towards the throat and in the nozzle. The sudden pressure increase at $x \approx -0.125$ m is caused by a small separation bubble located immediately downstream of the entrance to the throat section, which causes weak compression and expansion waves travelling downstream (small peaks and troughs in pressure and Mach number distributions). Behind the bow shock, the Mach number on the centerline drops to $M \approx 0.16$ which confirms the existence of an almost stagnant reservoir, Fig. 8b. The computed Mach number at the nozzle exit is $M \approx 2.5$ which agrees well with the value specified for the experiments.

Figure 9 shows the Mach number profiles at the nozzle exit, in the (x-y) and (x-z)-symmetry planes, respectively, obtained from the turbulent (SA and k-ε) nozzle computations. The value specified for the experiments along with the corresponding uncertainty range are included, for comparison. The agreement is good and the variation between the solutions for the different turbulence models is

Table 2 Inlet inflow conditions [12]

Parameter	Unit	Value
p_∞	kPa	32.77
T_∞	K	412
u_∞	m/s	1977
ρ_∞	kg/m^3	0.27704
M_∞	——	4.92
γ_∞	——	1.4
R_∞	J/kg K	287.1

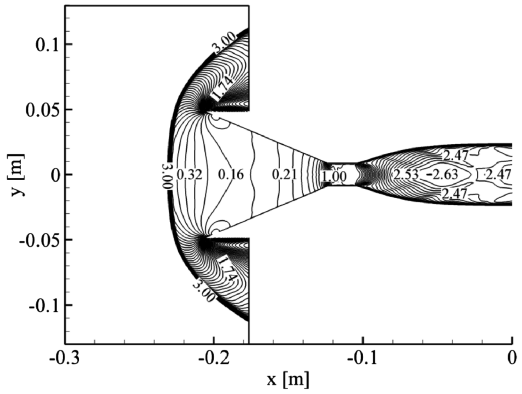

Fig. 7 Mach number distribution in the (*x*-*y*)-symmetry plane for a laminar inlet/nozzle computation.

negligible. Fluctuations in the vertical Mach number distribution (Fig. 9a) clearly indicate expansion and compression waves passing through the exit plane whereas the spanwise distribution is quite uniform. The expansion and compression waves originate from the aforementioned separation in the throat section. The Mach number profiles further reveal the existence of boundary layers on either wall which is distinctive of an internal flow. The consideration of an internal flow path, combined with the weak flow nonuniformity at the nozzle exit, distinguishes the present junction flow problem from previously investigated blunt fin induced SWBLIs. For the present case, the bow shock generated in front of the blunt strut injector reflects at the main wall above and below the strut and then again at the strut surface, interacting further with the fin–body interaction features and causing additional SWBLIs and SVIs within the flow domain. The following sections provide a detailed study of this particular internal junction flow problem.

B. Strut Injector Leading Edge and Upstream Plane of Symmetry

Figure 10 shows pressure distributions along the strut injector leading edge in the plane of symmetry ($\Phi = 0°$) and at various

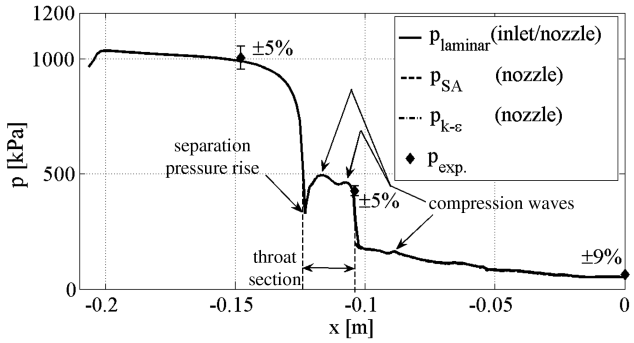

a)

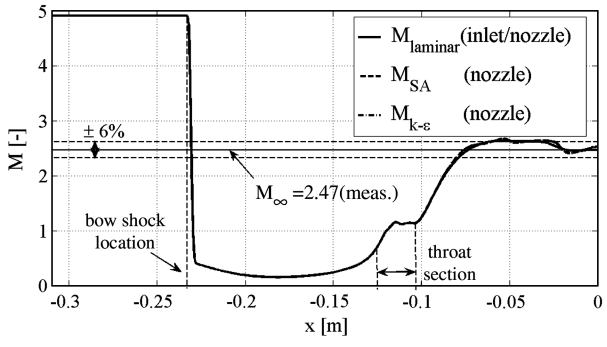

b)

Fig. 8 Streamwise, intake plus nozzle, flowfield distributions: a) wall pressure distribution along top wall in the (*x*-*y*)-symmetry plane and b) Mach number distribution on the centerline.

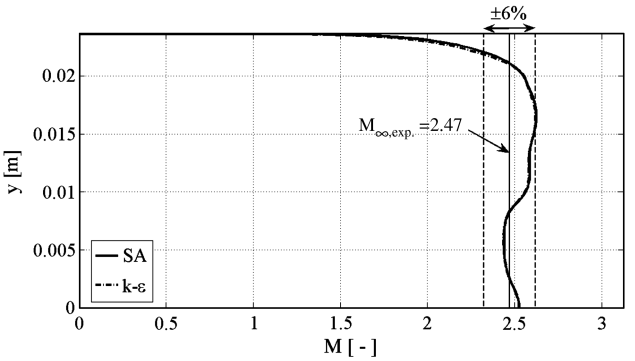

a)

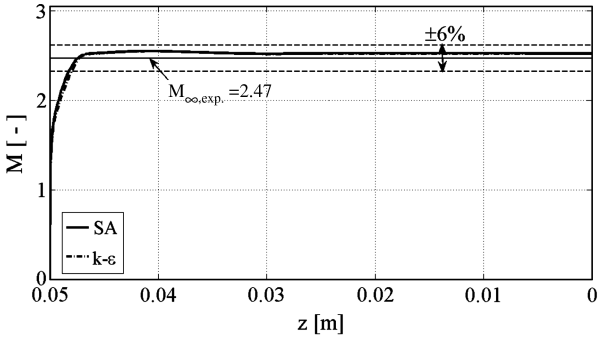

b)

Fig. 9 Turbulent (SA and *k*-*ε*) Mach number profiles at nozzle exit: a) (*x*-*y*)-symmetry plane and b) (*x*-*z*)-symmetry plane.

$\Phi =$ const. locations for both the SA and the k-ε solution. Φ denotes the angle to the horizontal of the strut nose wall normal measured from the leading edge. Note that $z = 0.05$ m corresponds to the side wall on which the fin–body interaction takes place. At $\Phi = 0$ and 45°, the pressure is normalized by the pitot pressure on the centerline at the location of the strut leading edge, which corresponds to the total pressure behind the normal shock at this location ($p_{t2,\mathrm{SA}} =$ 499.93 kPa and $p_{t2,(k\text{-}\varepsilon)} = 500.84$ kPa). At $\Phi = 90°$, the pressure distribution is normalized by the static pressure in the freestream in the (x-z)-symmetry plane, 6 mm upstream of the strut injector leading edge, averaged across the spanwise direction ($p_{\infty,\mathrm{SA}} = 60.5$ kPa and $p_{\infty,(k\text{-}\varepsilon)} = 60.6$ kPa). Spanwise fluctuations at this location were found to be negligible.

At $z \approx 0.0478$ m, a peak in pressure occurs at and near the leading edge ($\Phi = 0$ and 45°) which is followed by an extreme decline in pressure, far below p_{t2}. The subsequent sharp pressure rise is due to flow stagnation towards the side wall. At $\Phi = 90°$, the pressure drops even below the static pressure in the freestream reaching a minimum of $p/p_\infty \approx 0.7$. The pressure distribution along the symmetry line on the side wall is given in Fig. 11, in which the strut leading edge is at $x = -0.11$ m ($x = 0$ is the downstream end of the strut). The pressure is normalized by the wall pressure in the freestream, 6 mm upstream of the strut injector leading edge on the symmetry line. Both distributions (SA and k-ε solution) indicate a dip in pressure after the initial, separation pressure rise and a second smaller dip immediately upstream of the leading edge of the strut injector. The maximum upstream extent of the shock-induced separation on the side wall is $x/D \approx 1.9$, which agrees well with the results obtained in previous investigations of fin–body interactions, $x/D \approx 2$ [1,6,7].

For the sake of brevity, in the following, results are only presented for the SA solution. The results given so far as well as further comparisons (omitted here) of the SA and k-ε solutions for the injector domain computations neither revealed considerable variations of the location of separation on the side wall, nor in the overall flow structure within the flow domain and the interaction characteristics at the junction. Also the fine mesh results are only presented where notable variations appeared in the solution.

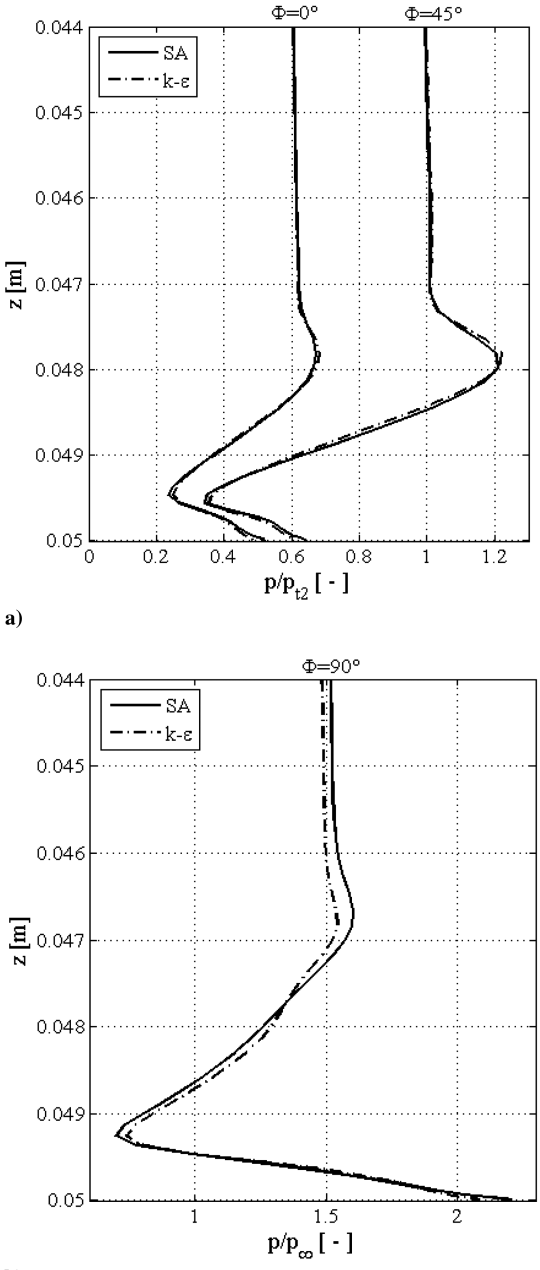

Fig. 10 Pressure distribution on injector leading edge: a) along $\Phi = 0°$ and $\Phi = 45°$ and b) along $\Phi = 90°$.

Figure 12 gives pressure and Mach number contours in the upstream plane of symmetry near the strut/side wall juncture. The pressure contours show a λ-shock structure which is formed by the intersection of the separation shock and the bow shock wave.

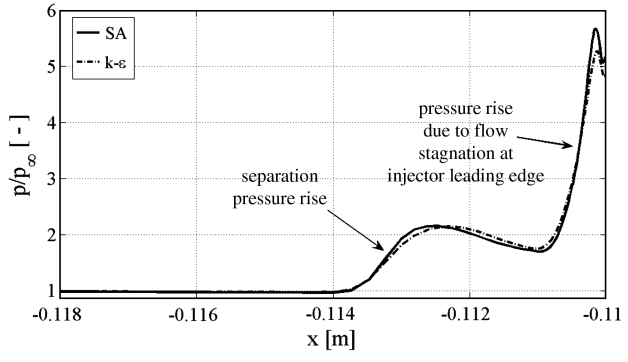

Fig. 11 Pressure distribution along symmetry line on side wall.

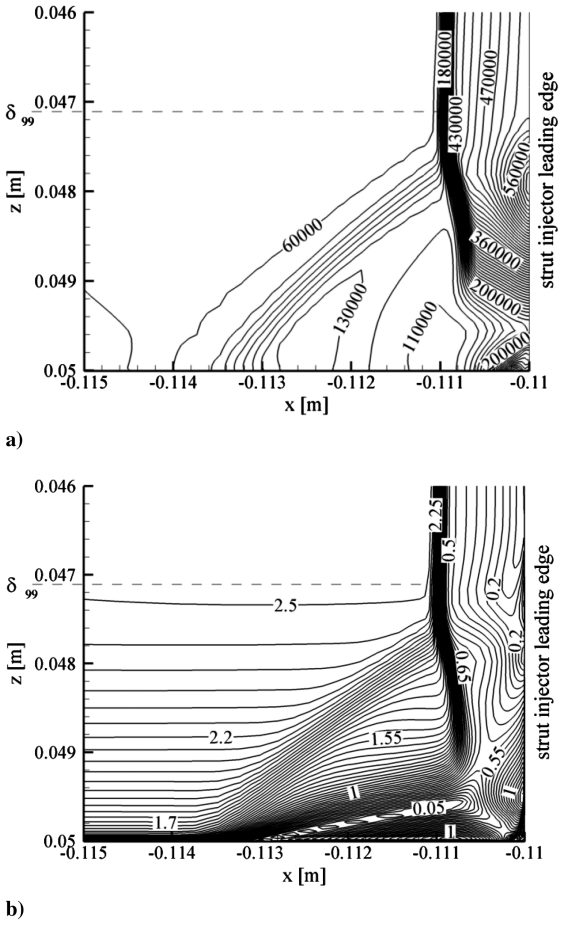

Fig. 12 Pressure and Mach number contours in the (*x*-*z*)-symmetry plane: a) pressure and b) Mach number.

Note that the separation shock is very weak and smeared and there is no sharp triple point at the intersection of the two shock waves. A peak and a low pressure region on the strut injector leading edge and a low pressure region on the side wall behind the separation shock are directly obvious. The dashed line in Figs. 12a and 12b marks the edge of the boundary layer, δ_{99}, on the side wall, which is defined as the location where $u/u_\infty = 0.99$, at $x = 0.114$ m. It can be seen that the interaction is completely embedded into the side wall boundary layer. An interesting feature in the Mach number distribution is the existence of two supersonic reversed flow regions; one on the strut injector leading edge and another one on the side wall with Mach numbers as high as 1.4 and 1.25, respectively. These coincide with the low pressure regions described before, and have also been observed by previous investigators of isolated fin–body junction flows [7]. The streamline pattern in the plane of symmetry in Fig. 13 indicates the formation of two counter-rotating vortices. The low momentum streamline (separation streamline) never stagnates on the side wall; hence no closed separation bubble exists. Instead, a large primary vortex originates from the separation point on the side wall and a second, much smaller vortex evolves from a separation on the injector leading edge very close to the junction. The primary vortex brings higher momentum fluid from the outer layers of the boundary layer into the separated region and hence accelerates the fluid in the corner. This results in the two supersonic reversed flow regions. Therefore, the separation on the leading edge is triggered by flow stagnation towards the side wall preceded by the vortex-induced acceleration of the corner flow. The dips in the pressure distribution along the side wall observed before and the low pressure region on the leading edge of the strut injector are thus attributable to the flow acceleration induced by the two vortices. The same observation was made by Hung and Buning [7] who concluded that the low pressure troughs are caused by the high velocity near the surfaces under the core of the vortex. Topologically, the saddle point/focus connections

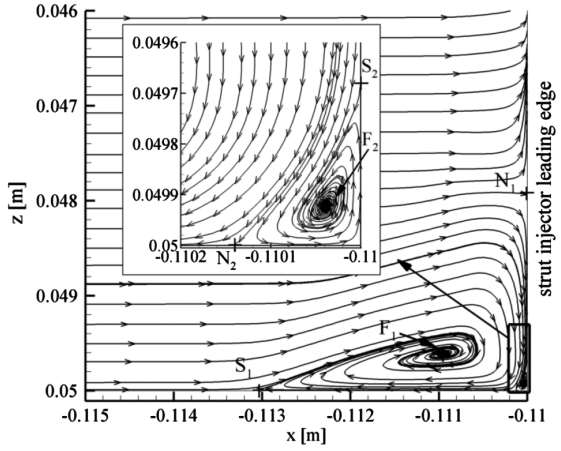

Fig. 13 Streamline pattern in the (x-z)-symmetry plane.

($S_1 - F_1, S_2 - F_2$) in Fig. 13 characterize the formation of horseshoe vortices [19]. The nodal points of attachment (N_1, N_2) are associated with flow stagnation on the injector leading edge and on the side wall, which explains the peak pressure region on the leading edge in Fig. 12a. The present injector/side wall junction flow features the characteristics of an isolated (no solid boundaries surrounding the flow domain) supersonic blunt fin–body interaction, at the present flow condition. Minor nonuniformities in the inflow conditions have negligible influence on the basic features of this particular type of SWBLI.

C. Details of the Full Flowfield

Details of the expansion around the blunt nose of the strut injector are illustrated in the three-dimensional view of the junction in Fig. 14, showing pressure contours in the symmetry plane and skin friction lines on the side wall and the strut injector surface. The pressure contours indicate the detached bow shock upstream of the injector leading edge and the λ-type shock pattern close to the side wall. As the vortices propagate downstream, around the shoulder, they imprint characteristic traces on the pattern of skin friction lines on the side wall and on the injector surface. The convergence of skin friction lines on the side wall marks the line of separation [19] which originates from a saddle point of separation at the foot of the separation shock in the plane of symmetry; hence, it is a global line of separation according to the classification given in [19]. The location of the saddle point coincides with the origin of the primary horseshoe vortex. Downstream of the separation line a divergence of skin friction lines indicates reattachment of the flow at the side wall. The diverging skin friction lines originate from a nodal point of attachment at the location of flow stagnation on the side wall. The strong surface pressure gradient associated with the reattachment process induces large velocity gradients close to the side wall, strongly increasing the skin friction and velocity there, which causes the divergence of the skin friction lines. Because of the presence of the horseshoe vortex the skin friction lines are then driven upstream forming the line of convergence. Further downstream, as the flow expands around the shoulder, no convergence of skin friction lines can be observed any more. Instead the skin friction lines on both sides of the separation line run parallel to each other. However, the line of convergence remains distinct on the side wall (as an artefact of the separation). Hence, it can be concluded that either the vortex lifted up from the surface or its strength is significantly weakened. It may also be conjectured that the overexpansion causes the vortex to become longitudinally stretched, which induces a downstream oriented pressure gradient that exceeds any lateral pressure gradient. In any case the lateral pressure gradient close to the surface, induced by the vortex, would be too small to significantly affect the distribution of skin friction lines in maintaining a converging pattern.

The line of separation on the strut injector surface starts from a saddle point of separation on the leading edge, which coincides with the point of separation in the plane of symmetry. Consequently, the separation is also of global type [19]. On the leading edge, the secondary vortex causes the convergence of skin friction lines by the same process as described for the separation line on the side wall. However, as the flow expands around the nose, another mechanism becomes influential. The pressure rise across the λ-shock structure is weaker as compared with adjacent regions further away from the side wall. Consequently, there exists a spanwise pressure gradient causing a lateral expansion away from the side wall and forcing the skin friction lines into the same direction. At the same time, the flow further away from the junction is expanded over the leading edge of the strut and subsequently runs against the flow which is displaced sidewards away from corner. Hence, the skin friction lines from both sides converge forming the line of separation and the flow lifts off the surface. The skin friction lines on the left side of the separation line emanate from a nodal point of attachment which corresponds to the stagnation point on the injector leading edge. The separation line is assumed to be the origin of a new stream surface which extends vertically into the flowfield and rolls up maintaining the secondary vortex downstream [19]. Similar to the line of separation on the side wall, further downstream of the nose, the skin friction lines on either side of the line of separation run parallel to each other and do not converge any more. The same reasoning as before can be applied here.

For the schematic depicted in Fig. 15, Fig. 16 shows computed Mach number contours near the junction in a sequence of planes normal to the strut injector leading edge. $\Phi = 0°$ denotes the (x-z)-symmetry plane. The range of the abscissa corresponds to a distance of 7 mm measured from the injector surface along the respective direction. The two supersonic reversed flow zones near the leading edge and near the side wall, which are attributed to the primary vortex, are clearly discernible. As the flow expands over the shoulder, the Mach number behind the bow shock increases substantially, while the Mach number near the side wall does not change significantly. The low speed tongue which represents the core region of the primary vortex (see previous section) remains about the same distance from the side wall within the boundary layer. Hence, the

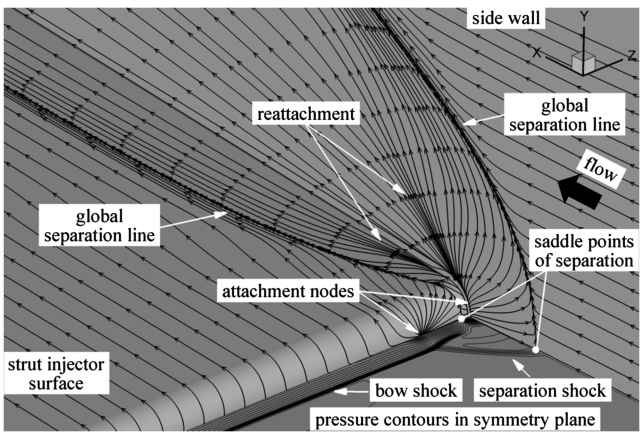

Fig. 14 Three-dimensional view of strut injector/side wall junction showing pressure contours in the symmetry plane and skin friction lines on the side wall and the strut injector surface.

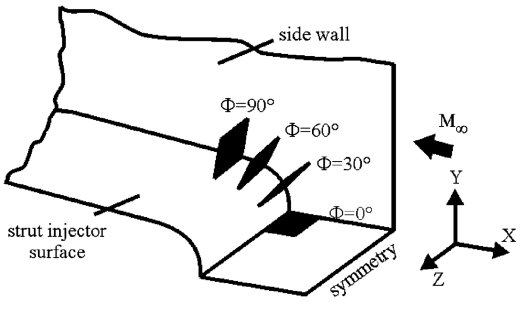

Fig. 15 Schematic showing planes represented in Fig. 16.

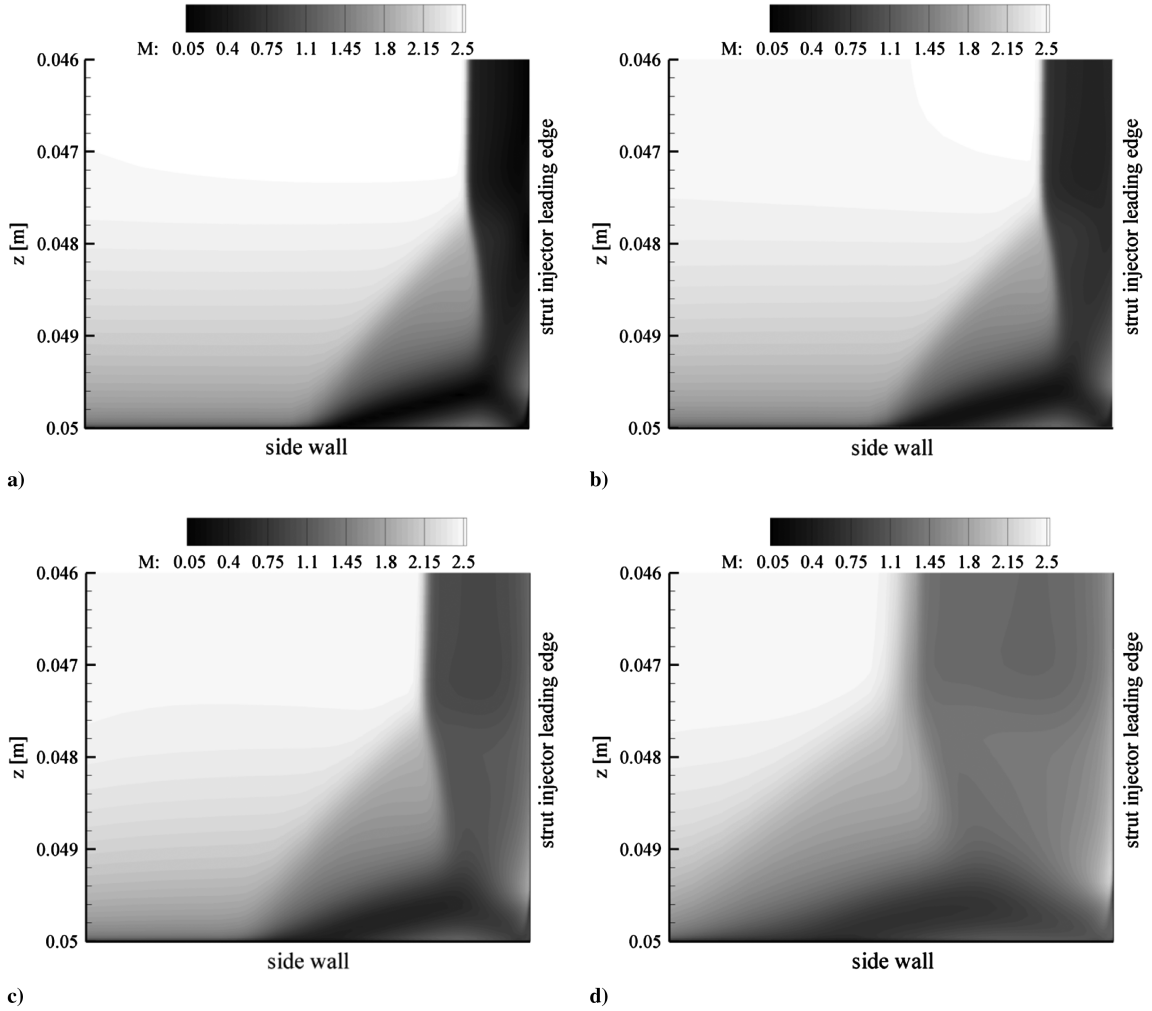

Fig. 16 Mach number contours in a sequence of planes around the strut injector leading edge: a) $\Phi = 0°$, b) $\Phi = 30°$, c) $\Phi = 60°$, and d) $\Phi = 90°$.

vortex does not penetrate into the inviscid flowfield and is subjected to intense viscous dissipation, as it propagates downstream. The same holds for the secondary vortex which is confined within the boundary layer on the strut surface.

A characteristic of the present internal flow is that the bow shock is able to reflect at the top wall and returns to the injector surface. The pattern of skin friction lines on the top wall, shown in Fig. 17, indicates a separation upon the impingement of the bow shock (convergence of skin friction lines), starting at $x \approx -0.086$ m and spanning the entire width. Immediately downstream of the separation, at $x \approx -0.084$ m, a divergence of skin friction lines marks the location of reattachment which suggests a closed separation bubble. The separation is initiated at the location where the shock wave disperses in the corner boundary layer. Hence, the resulting transverse pressure gradient forces the skin friction lines in the negative z-direction. Since the line of separation does not originate from a critical point, i.e., a saddle point or a nodal point, it is of local type [19]. A second separation bubble appears in the corner of the top wall and the side wall. In the corner the merger of the two boundary layers on the top wall and the side wall creates a region of significantly reduced momentum and kinetic energy. The pressure gradient imposed by the shock wave is sufficiently high to cause this second separation in the lower layers of the corner boundary layer. The distribution of wall shear stress across the separation in the (x-y)-symmetry plane in Fig. 18 shows that the size of the separation bubble, that spans the entire top wall, is highly sensitive to mesh resolution there. The fine mesh computation predicts a separation bubble almost twice the size as in the coarse mesh solution. Additionally, the coarse mesh solution features a considerably higher wall shear stress level at the location of separation as compared with the fine mesh solution. The decline to negative values then indicates the actual separation, and the subsequent increase of wall shear stress back to positive values is associated with the reattachment process. The same sensitivity on mesh resolution was observed for the shock reflection at the injector surface.

As the reflected shock approaches the injector surface, it is curved towards the surface due to the interaction with the expansion fan generated at the expansion corner of the strut. By this process, the shock strength increases locally, imposing an increased adverse pressure gradient on the flow and the boundary layer on the strut surface. Figure 19 illustrates computed skin friction lines on the injector surface for both the coarse mesh and the fine mesh

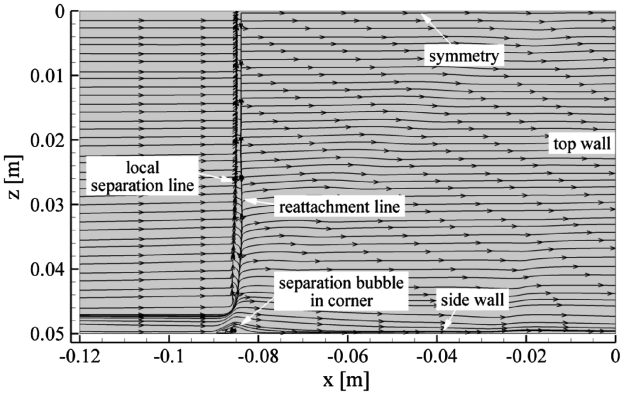

Fig. 17 Pattern of skin friction lines on the top wall.

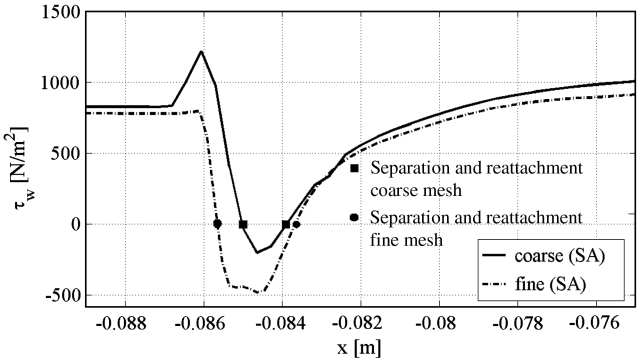

Fig. 18 Wall shear stress distribution across separation region on the top wall in the (*x*-*y*)-symmetry plane; comparison between coarse and fine mesh solution.

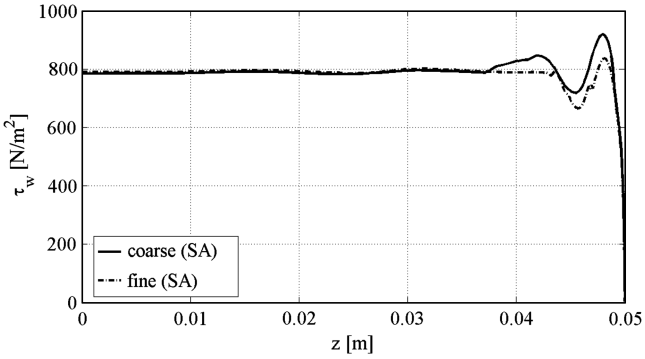

Fig. 20 Spanwise distribution of wall shear stress on the strut injector surface; comparison between coarse and fine mesh solution. (Note: separation was only observed for the fine mesh solution.)

computation. It can be seen that the fine mesh solution (b) features a small separated region (convergence of skin friction lines) upon the impingement of the reflected shock wave which was not resolved by the coarse mesh computation. This may be attributed to the enhanced resolution of the boundary layer in the corner of the injector surface and the side wall. Also, recall that the fine mesh solution indicated a greater separation on the top wall which results in a stronger reflected shock wave. Immediately downstream of the separation a divergence of skin friction lines indicates reattachment of the flow at the injector surface. Why is the separation confined to only a small region? It may be assumed that the boundary layer in the vicinity of the primary separation line (see Fig. 19), which originates from the leading edge, consists of lower momentum fluid close to the surface as compared with the undisturbed flow further away from the side wall. Hence, the boundary layer in this region is weakened and possesses not enough kinetic energy to overcome the adverse pressure gradient induced by the incident shock wave. The spanwise distribution of wall shear stress on the injector surface plotted immediately upstream of separation, at $x \approx -0.056$ m, confirms this argument, Fig. 20. Towards the side wall, the wall shear stress drops to a minimum arising from a smaller velocity gradient at the wall and reduced kinetic energy of the flow close to the surface as compared with adjacent regions. Along the remaining spanwise direction the distribution is quite uniform suggesting a larger velocity gradient at the wall; hence, the boundary layer is less susceptible to separation there. Close to the side wall, the fine mesh solution reveals a lower shear stress level than the coarse mesh solution which is obviously attributed to enhanced mesh resolution. This explains the existence of the separated region in the fine mesh solution, since the boundary layer is less stable in this case.

D. Downstream Development of Vortices

The interesting question is now, what is the impact of the shock structures within the strut domain on the development of the vortices? Figure 21 shows a sequence of spanwise *x*-vorticity contours (streamwise component). Three-dimensional volume streamlines, released at the inflow plane immediately adjacent to the side wall and within the symmetry plane, illustrate the formation and downstream propagation of the vortices. It can be seen that the primary and the secondary vortex are associated with concentrated regions of increased streamwise vorticity near the side wall and close to the injector surface, respectively. Along the injector surface, the secondary vortex maintains the same sense of rotation, i.e., positive about the *x*-axis. However, its strength is significantly reduced upon its downstream progression. The streamlines indicate that the vortex remains confined close to the surface. Therefore, the weakening of the vortex may be attributed to cumulative viscous dissipation within the boundary layer on the injector surface.

The primary vortex extends vertically along the side wall and is gradually reorientated towards the streamwise direction rotating counter-clockwise, i.e., negative about the *x*-axis. The sequence of Mach number contours around the nose of the strut injector presented

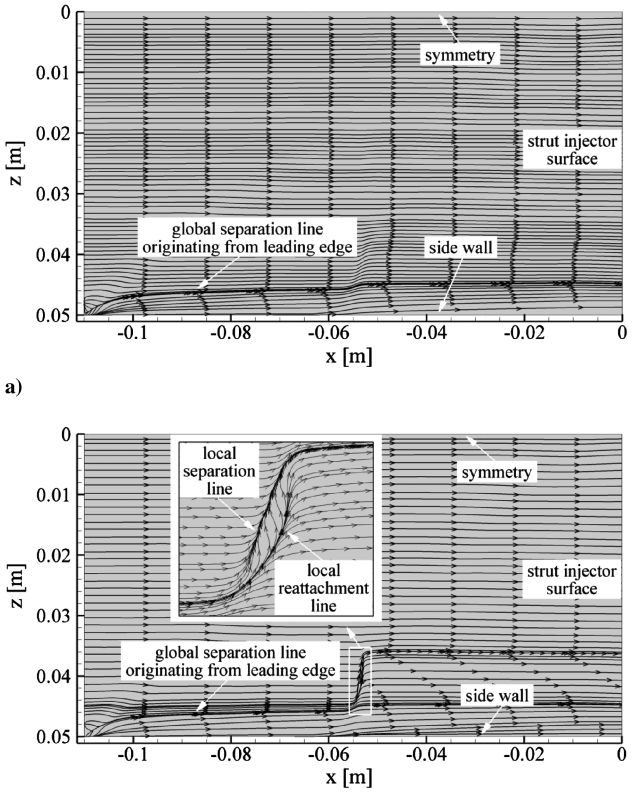

Fig. 19 Pattern of skin friction lines on the strut injector surface: a) coarse mesh solution and b) fine mesh solution.

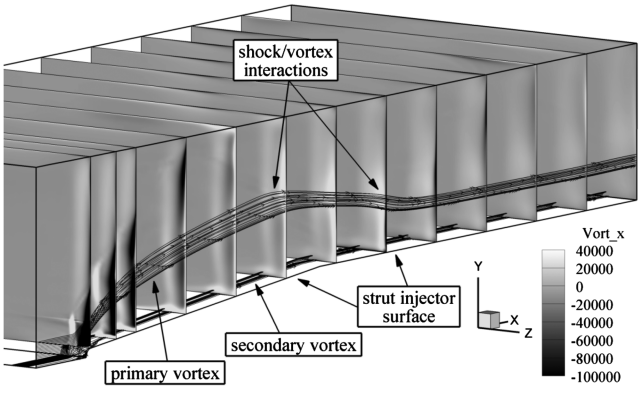

Fig. 21 Sequence of spanwise *x*-vorticity contours and three-dimensional volume streamlines illustrating downstream propagation of vortices.

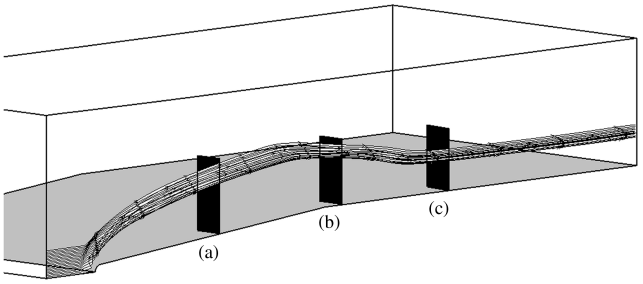

Fig. 22 Schematic showing planes represented in Fig. 23.

in Fig. 16 showed that the vortex remains confined within the side wall boundary layer. Hence, it is subjected to intense viscous dissipation, as described before. Additionally, the extension of the streamlines, caused by the expansion around the nose of the injector, decreases the entrainment of boundary layer vorticity into the vortex and increases viscous dissipation [20]. As the vortex encounters the reflected shock wave (downward deflection of streamlines), the sudden appearance of a region of increased positive x-vorticity indicates a reversal of the sense of rotation. Upon the interaction with the reflected shock wave coming from the injector surface (upward deflection of the streamlines), the x-vorticity component is significantly reduced. However, the strength of the second reflected shock wave is obviously insufficient to cause a further reversal of the sense

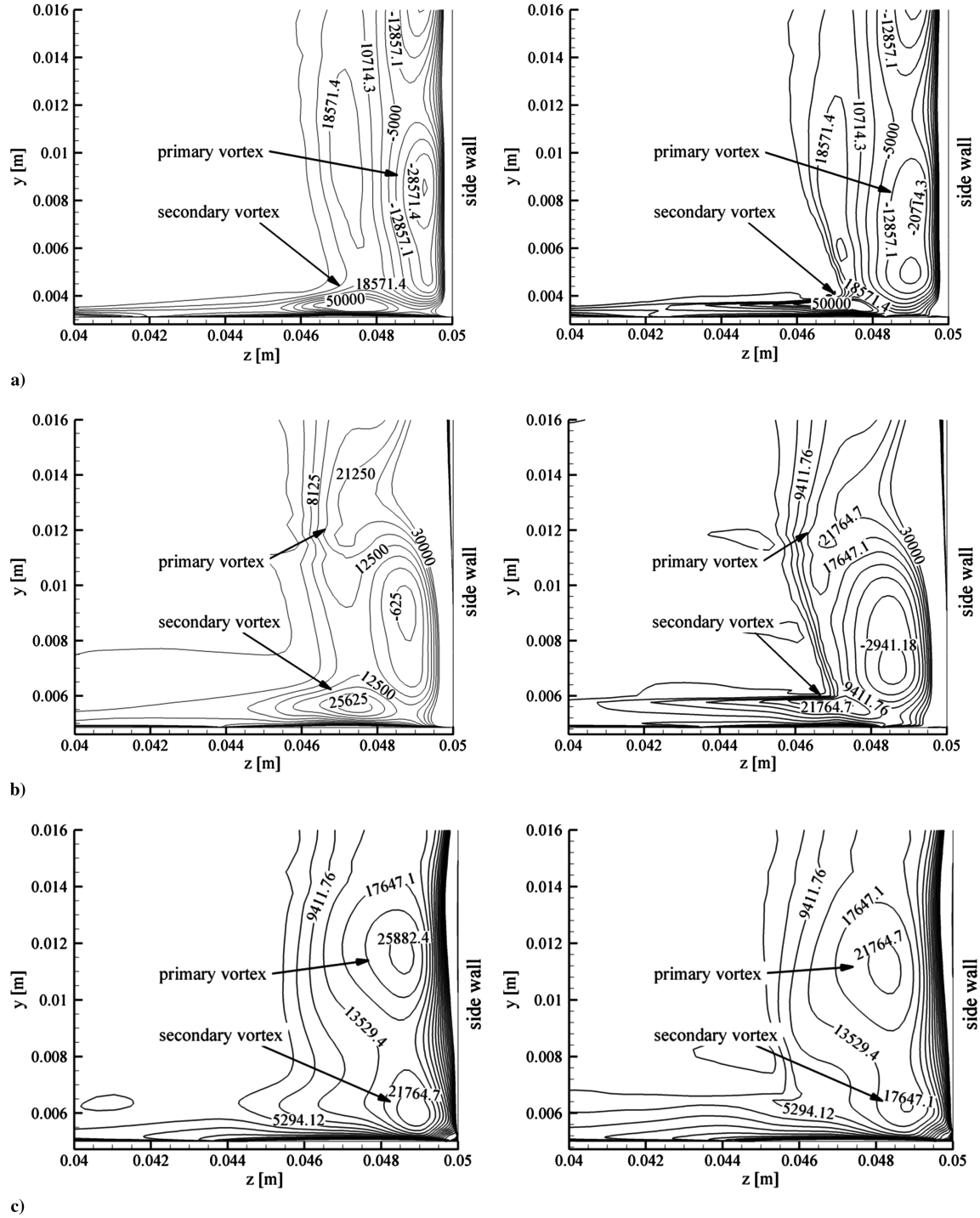

Fig. 23 Selected spanwise slices showing x-vorticity contours adjacent to the side wall for the SA solution (left) and the k-ε solution (right): a) $x = -0.085$ m before first SVI, b) $x = -0.065$ m after first SVI, and c) $x = -0.038$ m after second SVI.

of rotation. The schematic in Fig. 22 shows the locations of selected spanwise slices for which Figs. 23a–23c give a more precise illustration of these phenomena. The latter presents these selected spanwise slices showing x-vorticity contours adjacent to the side wall before the first SVI (a), in between the first and the second SVI (b), and after the second SVI (c) for both the SA and the k-ε solution. At first, the primary vortex is characterized by a region of negative streamwise vorticity which disappears upon the first SVI, and positively oriented streamwise vorticity is induced instead. The second SVI then results in a weakening of the vortex without a further reversal of its sense of rotation. In contrast to that, the small secondary vortex near the injector surface maintains the same sense of rotation downstream. In general, it can be stated that the k-ε computation predicts a slightly weaker vortex before and after each SVI. It may be concluded that the SVIs act to despin the vortex, i.e., oppositely orientated vorticity is induced, upon which its sense of rotation is reversed, and hence dissipate streamwise vorticity. For the present case, the dominant influence causing this reversal is considered to be due to barotropic effects across the reflected shock wave. Barotropic effects occur whenever pressure and density gradients are not aligned. To the end of the flow domain, the vorticity decreases progressively under the influence of viscous dissipation in the side wall boundary layer and no pronounced regions of increased vorticity are discernible any more.

V. Conclusions

Three-dimensional simulations of an internal supersonic scramjet flow encountering a fin–body type protuberance, at a blunt strut injector spanning the flow duct, have been conducted. The computed interaction phenomena near the strut leading edge resemble the pattern of an isolated fin–body junction flow, at the present flow condition. The shock-induced separation on the side wall of the scramjet duct results in the formation of a λ-shock structure and two separation vortices; a large primary vortex close to the side wall, and a second much smaller counter-rotating vortex on the strut injector leading edge. Further SWBLIs occur upon the reflections of the bow shock at the top wall and at the strut injector surface. These interactions displayed a strong sensitivity to mesh resolution. Downstream of the leading edge, both vortices are significantly weakened due to cumulative viscous dissipation, as they remain confined within the corresponding boundary layers on the side wall and the injector surface. Additionally, the interactions of the primary vortex with the shock reflections act to despin the vortex by producing oppositely orientated vorticity causing a reversal of its sense of rotation due to barotropic effects across the reflected shock wave and hence dissipate streamwise vorticity. The occurrence of these SVIs distinguishes the present flow problem from previously studied isolated fin–body junction flows and thus helps to fill in a gap in the understanding of three-dimensional separated flows in the context of an internal flowfield, involving multiple SWBLIs of different types.

Acknowledgment

The computations of the present work have been performed on the computing system provided by Australia's National Computational Infrastructure National Facility.

References

[1] Dolling, D. S., and Bogdonoff, S. M., "Blunt Fin-Induced Shock Wave/Turbulent Boundary-Layer Interaction," *AIAA Journal*, Vol. 20, No. 12, 1982, pp. 1674–1680. doi:10.2514/3.8003

[2] Dolling, D. S., "Comparison of Sharp and Blunt Fin-Induced Shock Wave/Turbulent Boundary-Layer Interaction," *AIAA Journal*, Vol. 20, No. 10, 1982, pp. 1385–1391. doi:10.2514/3.7982

[3] Price, A. E., and Stallings, R. L., "Investigation of Turbulent Separated Flow in the Vicinity of Fin Type Protuberances at Supersonic Mach Numbers," NASA TN D-3804, 1967.

[4] Brusniak, L., and Dolling, D. S., "Physics of Unsteady Blunt-Fin-Induced Shock Wave/Turbulent Boundary Layer Interactions," *Journal of Fluid Mechanics*, Vol. 273, 1994, pp. 375–409. doi:10.1017/S0022112094001989

[5] McMaster, D. L., and Shang, J. S., "A Numerical Study of Three-Dimensional Separated Flows Around a Sweptback Blunt Fin," AIAA Paper 88-0125, 1988.

[6] Lakshmanan, B., and Tiwari, S. N., "Study of Supersonic Intersection Flowfield at Modified Wing-Body Junctions," *AIAA Journal*, Vol. 31, No. 5, 1993, pp. 877–883.

[7] Hung, C.-M., and Buning, P. G., "Simulation of Blunt-Fin-Induced Shock-Wave and Turbulent Boundary-Layer Interaction," *Journal of Fluid Mechanics*, Vol. 154, 1985, pp. 163–185. doi:10.1017/S0022112085001471

[8] Vos, J. B., Duquesne, N., and Lee, H. J., "Shock Wave/Boundary Layer Interaction Studies Using the NSMB Flow Solver," *Proceedings of the Third European Symposium on Aerothermodynamics for Space Vehicles, 24–26 November 1998*, ESA SP-426, ESTEC, Noordwijk, The Netherlands, Dec. 1998.

[9] Hung, C.-M., "Computation of Separation Ahead of Blunt Fin in Supersonic Turbulent Flow," NASA TM-89416, 1986.

[10] Hung, C.-M., "Simulation of Glancing Shock Wave and Boundary Layer Interaction," NASA TM-102233, 1989.

[11] Hung, C.-M., "Computation of Navier–Stokes Equations for Three-Dimensional Flow Separation," NASA TM-102266, 1989.

[12] Boyce, R. R., Paull, A., Stalker, R. J., Wendt, M., Chinzei, N., and Miyajima, H., "Comparison of Supersonic Combustion Between Impulse and Vitiation-Heated Facilities," *Journal of Propulsion and Power*, Vol. 16, No. 4, 2000, pp. 709–717. doi:10.2514/2.5631

[13] Boyce, R. R., Paull, A., and Stalker, R. J., "Unstarted Inlet for Direct-Connect Combustor Experiments in a Shock Tunnel," *Journal of Propulsion and Power*, Vol. 16, No. 4, 2000, pp. 718–720. doi:10.2514/2.5633

[14] Goldberg, U., Batten, P., Palaniswamy, S., Chakravarthy, S., and Peroomian, O., "Hypersonic Flow Predictions Using Linear and Nonlinear Turbulence Closures," *Journal of Aircraft*, Vol. 37, No. 4, 2000, pp. 671–675. doi:10.2514/2.2650

[15] Reinartz, B., Ballmann, J., Brown, L., Fischer, Ch., and Boyce, R., "Shock Wave/Boundary Layer Interactions in Hypersonic Intake Flows," Second European Conference for Aerospace Sciences, Brussels, 2007.

[16] McGuire, J. R., "Ignition Enhancement for Scramjet Combustion," Ph.D. Dissertation, University of Queensland, Brisbane, Queensland, Australia, 2007.

[17] Goldberg, U., Peroovian, O., Chakravarthy, S., and Sekar, B., "Validation of CFD++ Code Capability for Supersonic Combuster Flowfields," AIAA Paper 97-3271, 1997.

[18] "Gridgen User Manual," Ver. 15, Vol. 1, Pointwise, Fort Worth, TX, 2005.

[19] Tobak, M., and Peake, D. J., "Topology of Three-Dimensional Separated Flows," *Annual Review of Fluid Mechanics*, Vol. 14, 1982, pp. 61–85. doi:10.1146/annurev.fl.14.010182.000425

[20] Praisner, T. J., and Smith, C. R., "The Dynamics of the Horseshoe Vortex and Associated Endwall Heat Transfer, Part 2: Time-Mean Results," *Journal of Turbomachinery*, Vol. 128, No. 4, 2006, pp. 755–762. doi:10.1115/1.2185677

C. Segal
Associate Editor